Surface diffuse discharge mechanism of well-aligned atmospheric pressure microplasma arrays*

Ren-Wu Zhou(周仁武)[1], Ru-Sen Zhou(周儒森)[2], Jin-Xing Zhuang(庄金星)[3], Jiang-Wei Li(李江炜)[1], Mao-Dong Chen(陈茂冬)[1], Xian-Hui Zhang(张先徽)[1,†], Dong-Ping Liu(刘东平)[1,4], Kostya (Ken) Ostrikov[5,6], and Si-Ze Yang(杨思泽)[1]

[1] *Fujian Key Laboratory for Plasma and Magnetic Resonance, School of Physics and Mechanical & Electrical Engineering, Xiamen University, Xiamen* 361005, *China*

[2] *Department of Chemical and Biochemical Engineering, College of Chemistry and Chemical Engineering, Xiamen University, Xiamen* 361005, *China*

[3] *Xiamen Jueshi Language Training Center, Xiamen* 361005, *China*

[4] *Liaoning Key Laboratory of Optoelectronic Films & Materials, School of Physics and Materials Engineering, Dalian Nationalities University, Dalian* 116600, *China*

[5] *School of Chemistry, Physics and Mechanical Engineering, Queensland University of Technology, Brisbane, Queensland* 4000, *Australia*

[6] *CSIRO, Materials Science and Engineering, P. O. Box* 218, *Lindfield, NSW* 2070, *Australia*

(Received 1 November 2015; revised manuscript received 10 December 2015; published online 25 March 2016)

A stable and homogeneous well-aligned air microplasma device for application at atmospheric pressure is designed and its electrical and optical characteristics are investigated. Current-voltage measurements and intensified charge coupled device (ICCD) images show that the well-aligned air microplasma device is able to generate a large-area and homogeneous discharge at the applied voltages ranging from 12 kV to 14 kV, with a repetition frequency of 5 kHz, which is attributed to the diffusion effect of plasma on dielectric surface. Moreover, this well-aligned microplasma device may result in the uniform and large-area surface modification of heat-sensitive PET polymers without damage, such as optimization in hydrophobicity and biocompatibility. In the biomedical field, the utility of this well-aligned microplasma device is further testified. It proves to be very efficient for the large-area and uniform inactivation of *E. coli* cells with a density of $10^3/\text{cm}^2$ on LB agar plate culture medium, and inactivation efficiency can reach up to 99% for 2-min treatment.

Keywords: surface diffusion, intensified charge coupled device, surface modification, bacterial inactivation

PACS: 52.50.Dg, 87.80.–y, 52.77.–j **DOI:** 10.1088/1674-1056/25/4/045202

1. Introduction

Atmospheric pressure cold microplasma has recently attracted much attention especially in biomedical application (plasma sterilization,[1] living tissue treatment,[2] induction of apoptosis,[3] cancer therapy[4]) and material processing (surface modification,[5,6] processing,[7] nanotech application,[8]) due to its high plasma density, low gas temperature, high discharge stability, and the simplicity of the experimental set-up. However, in order to obtain stable microplasmas at atmospheric pressure, the feed gases used for most plasma devices are noble gases, such as helium or argon, which adds to the difficulties for widespread application. Briefly, it is difficult to generate a stable and homogeneous air discharge at atmospheric pressure due to the high breakdown voltage or the non-homogeneity of filamentary discharges.[9–13]

However, the utilization of atmospheric air can greatly reduce the complexity of the device and enhance the production of reactive species, mainly including (i) negative particles (e^-, O^-, and O_2^-); (ii) positive particles N_2^+, N_4^+, O^+, O_2^+, O_4^+, H^+, H_2^+, OH^+, NO^+, and NO_2^+; (iii) atoms N, O, and H; (iv) molecules N_2, O_2, O_3, OH, HO_2, and NO_x. For these various plasma-activated neutrals, O and OH radicals and nitrogen-containing species (reactive nitrogen species (RNS)) have been presumed to play a reasonable role in the plasma inactivation of microorganisms.[14–16] Therefore, it is preferable to directly utilize the air, thereby leading to cost savings for industrial and biomedical uses.

The small size of the atmospheric pressure air microplasma also prevents it from being used in some areas such as plasma inactivation and decontamination of reusable medical tools.[1,17] Several researches are under way to overcome this difficulty. Eden *et al.* pointed out that microcavity plasmas had advanced rapidly in surpassing several milestones, primarily with respect to electron density and cavity geometries, and some new avenues of research with noble gases, such as Ne, Xe or gas mixture, at a total pressure of several hundred Torrs were established.[18] For this purpose, our research team has conceived another effective approach and contrived

*Project supported by the Natural Science Foundation of Fujian Province, China (Grant No. 2014J01025), the National Natural Science Foundation of China (Grant No. 11275261), the Natural Science Foundation of Guangdong Province, China (Grant No. 2015A030313005), and the Fund from the Fujian Provincial Key Laboratory for Plasma and Magnetic Resonance, China.

†Corresponding author. E-mail: zhangxh@xmu.edu.cn

© 2016 Chinese Physical Society and IOP Publishing Ltd

a novel well-aligned microplasma array.

The microplasma device consists of 6×6 well-aligned, stable microplasma jets formed near the ends of hollow optical fibers sealed at one end at room temperature. The unique advantage of this device is that these microplasma jets with the polarity effect of discharge can aggregate along the surface of dielectric and form a large-area uniform surface plasma. The detailed schematic of this plasma device is illustrated below, and its electrical and optical characteristics are analyzed based on experimental data. Moreover, as a case of application, this well-aligned air plasma is used for large-area uniform surface modification of polyethylene terephthalate (PET) polymers and plasma inactivation of *E. coli* cells at room temperature.

2. Experiments

2.1. Plasma reactor and multiglow mode discharge

The schematic diagram of the microplasma array is shown in Fig. 1(a). The plasma device is mainly composed of microplasma jet units housed in a glass cup. In each microplasma jet unit, two hollow fibers, with the inner diameters of 200 μm and 1500 μm respectively, are used to generate the air microplasma inside the larger hollow fiber. The distances between per two microplasma jet units in horizontal and vertical directions are both 5.0 mm as shown in Fig. 1(c). A 200-μm-thick tungsten wire, acting as one high-voltage electrode, is inserted into the 200-μm-inner-diameter fiber with one sealed end which is fixed and centered on the Al_2O_3 plate below. The 200-μm-inner-diameter fiber is inserted into the 1500-μm-inner-diameter fiber fixed on the Al_2O_3 plate above, and the separation between their ends is fixed to be 1 mm. In this study, 6×6 microplasma jet units are uniformly distributed inside the glass cup with an inner diameter of 70 mm. The air feed gas is added into the 36 microplasma jet units at a flow rate of 4.0 standard liter per minute (SLM). In theoretic trials, the grounded indium tin oxide coated quartz for mechanism research is 2 mm in thickness. When it comes to practical application, the grounded stainless-steel electrode is covered by a 2-mm-thick quartz plate. When a sinusoidal AC high-voltage is applied between the electrodes, a visually large-area and uniform discharge is generated on the dielectric surface. The power supply is capable of providing bipolar AC output with the peak voltage (V_P) of 0 kV–20 kV at an AC frequency of 1.0 kHz–15 kHz. Figure 1(b) shows the photographs of well-aligned air plasma generated at $V_{PP} = 14$ kV, acquired from the frontage and broadside of discharge area respectively.

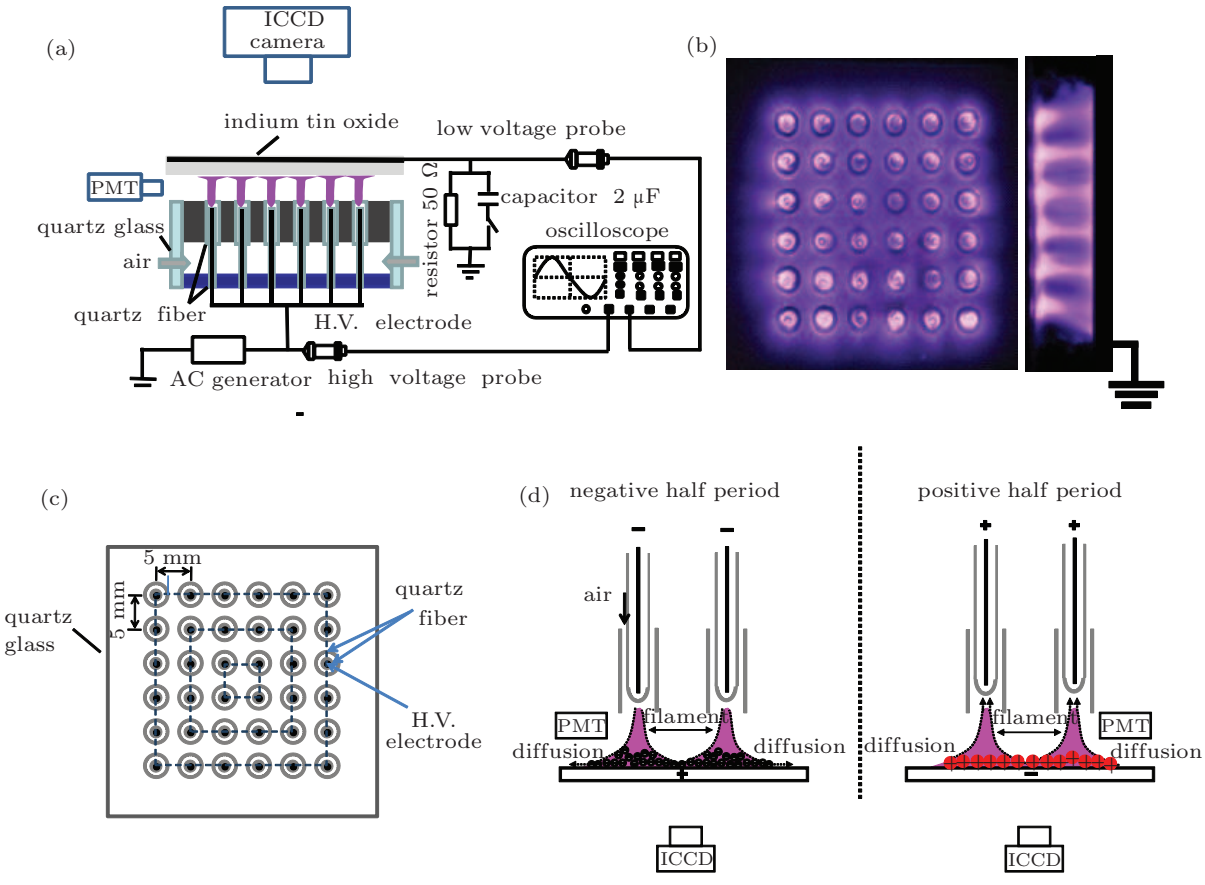


Fig. 1. (color online) Schematic diagram of the experimental setup used in this study. (a) Cross-sectional view of the microplasma array device; (b) photographs of well-aligned air plasma generated at $V_{PP} = 14$ kV, acquired from the frontage and broadside of discharge area respectively; (c) top view of the plasma device; (d) discharge and diffusion model of the microplasma jet unit as recorded with the PMT and ICCD camera.

2.2. Analytical methods

Applied voltage and discharge current are simultaneously measured by using a Tektronix DPO5024 digital oscilloscope with a 1:1000 H.V. probe (Tektronix P6015A) and a Tektronix P2220 current probe. Measurements for the charges across this capacitor and the applied voltage across the discharge device result in a Lissajous figure, which is used to calculate the discharge power.[19,20] Contact angle measurements are performed by using the sessile drop method with a contact angle goniometer (Phoenix 300, SEO) at an ambient temperature after 5.0-μl water drops have been applied to the surface of samples. Contact angle measurements of the treated polymers immediately follow plasma treatment with a delay of 3 min–5 min. For each sample, at least three drops are placed at different locations on the large-area polymer. Surface chemical compositions of PET polymers are analyzed by XPS. These analyses are performed on a Physical Electronics PE5800 ESCA/Auger electron spectroscopy system. Survey scans (0 eV–1000 eV), acquired with an analyzer pass energy of 93.9 eV, are used to determine elemental compositions. A photoelectron take-off angle of 45° is used for all spectra. High-resolution C1s spectra are deconvoluted to analyze the C bonding environment at the surfaces of treated polymers.

Photoelectron multiplier tubes (PMTs) (Hamamatsu CR131) are used to study the optical emission from the well-aligned microplasmas, placed at 25 mm away from the broadside of discharge area. The output of the PMTs, the voltage and current waveforms are simultaneously recorded by Tektronix DPO 5024. In the front part of PMT, there are two slits each with 1 mm in width and 20 mm in thickness, and they are separated by a distance of 100 mm. In addition, an ICCD camera (ANDOR, iStar DH712) is fixed at 50 cm above the discharge region to capture the discharge propagation processes. The ICCD camera is triggered by a square wave with a peak value of 2.6 V, which is generated by the digital delay generator (DG645). Also, the digital delay signals are recorded simultaneously by using Tektronix DPO5024 oscilloscope. Optical emission spectra from the discharge region are obtained by using an Andor SR-750i grating monochromator (grating groove at 2400 lines/mm and glancing wavelength at 300 nm). After the diffraction of the grating, the output light signal is converted into digital signals by CCD camera and stored in the connected computer.

2.3. Experimental procedures

During the material modification, the 200-μm-thick PET (Teijin company, Japan) sample is placed on the quartz plate. The PET sample with a melting point of 254 °C is amorphous. The plasma device is fixed at 1 mm above the sample for performing this plasma treatment. The adhesion of blood platelets on untreated or plasma-treated PET polymers is investigated and evaluated by using SEM (Hitachi S4800). The platelet-rich blood plasma from a healthy donor is diluted 10 times with pure water. After being incubated for 2 h, the sample is washed by phosphate buffered saline (PBS) several times to remove loosely-clung platelets. The PET sample is then exposed to 25% glutaraldehyde for 2 h for fixation, dehydrated with alcohol, then dealcoholizated with isoamyl acetate solution and subsequently dried under ambient conditions.

The *E. coli* cells with a density of $10^3/\text{cm}^2$ on LB agar plate culture medium are used to investigate the inactivation efficiency of the visually large-area uniform discharge. A single colony of *E. Coli* is inoculated into 200 ml of LB liquid medium (Tryptone: 2 g, Yeast Extract: 1 g, distilled water: 200 g, pH = 7.2) and is cultivated on the shaking table with a rotation speed of 150 rpm at 28 °C. For plasma inactivation treatments, 100 μl of the *E. coli* culture is deposited on the LB agar plate culture medium to make a sample have a density of $10^3/\text{cm}^2$. During the bacterial treatment, the petri-dish containing *E. coli* cells is grounded. The plasma device is fixed at 1 mm above the sample for performing this plasma treatment. The treatment time varies from 10 s to 2.0 min. For all inactivation and modification treatments, the air flow rate and V_P are kept to be 4 SLM and 14 kV respectively. Likewise, for the plasma-untreated (control) sample cultivation, the 4 SLM air feed gas is added into the well-aligned plasma device, and kept for 2 min for comparison. Following this, the plasma-treated culture media containing *E. coli* cells are incubated for 24 h in a 37-°C thermostatic container for observation while the untreated one is used as a control sample. Afterward, cellular colonies are counted to calculate the inactivation efficiency in the treated area. The detailed process is similar to that reported in our previous work.[21] All the experiments reported are repeated three times, and all the data obtained under the same experimental condition are repeatable and consistent.

3. Results and discussion

3.1. Electrical and optical characteristics of the microplasma array device

Figures 2(a)–2(d) show the applied voltage and current waveforms of the atmospheric pressure microplasma array device, obtained at $V_\text{P} = 10$ kV, 12 kV, 14 kV, and 15 kV, respectively. The measurements are performed at an air flow rate of 4 SLM and with a fixed repetition frequency of 5 kHz. It is clear that plasma is produced by strong pulsed microdischarge, and the duration of pulsed discharges in most cases is tens of nanoseconds, a phenomenon that is referred to as filamentary barrier discharge.[22] Furthermore, the directions and amplitude of these filament currents are different in the negative high voltage (NHV) and positive high voltage (PHV) half-cycles. Filamentary discharges in the PHV cycle are much stronger

than the ones in the NHV cycle. The above-observed differences between two half-cycles could be explained by the polarity effect for a needle-shaped electrode configuration.[23–25] The electrons and ions behave differently on the outer surface of 200-μm-inner-diameter fiber during their propagation. The formation of atmospheric pressure microplasmas can be explained by the streamer mechanism, where UV ionization may be important for its propagation.[26–28] Obviously, the discharge current is significantly influenced by the applied voltage. In the initial discharge state with an applied voltage of 10 kV in Fig. 2(a), the amplitude of the filament discharge current varies from 8 mA to 39 mA. The duration of the discharge process is about 42.2 μs in the NHV cycle and about 44.5 μs in the PHV cycle. And the time lags of the adjacent filamentary currents vary randomly from about 240 ns to 5.9 μs. With V_P increasing from 10 kV to 15 kV, the intensity of the discharge currents and the density of filament currents in the discharge process are both greatly improved, and the time lags of the adjacent filamentary currents decrease as shown in Figs. 2(b)–2(d). This result also indicates an improvement in the density of this well-aligned microplasma when voltage rises from 10 kV to 15 kV.

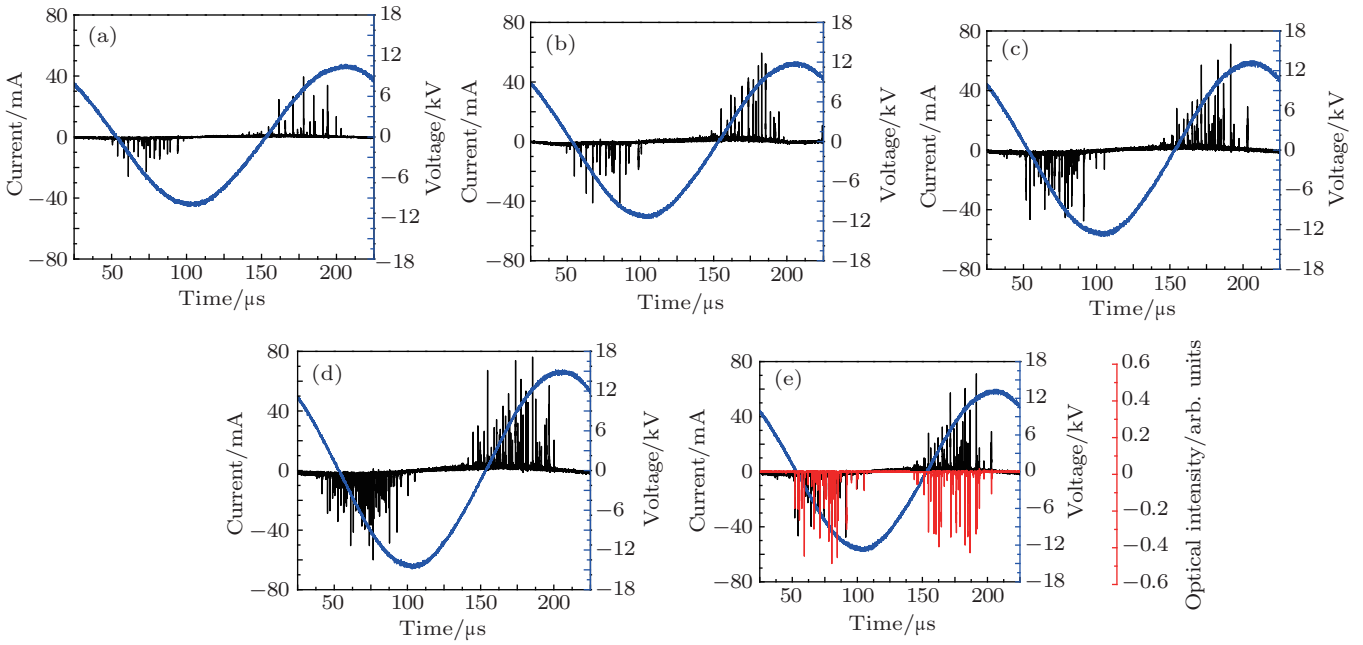


Fig. 2. (color online) Typical applied voltage and current waveforms obtained at V_P = (a) 10 kV, (b) 12 kV, (c) 14 kV, (d) 15 kV. (e) Optical intensity monitored at the side of well-aligned microplasma arrays by PMT, which is recorded with the voltage and current waveforms simultaneously. The measurements are performed at an air rate of 4 SLM and a frequency of 5 kHz.

To investigate the discharge characteristics of the well-aligned microplasma array, the high-speed ICCD camera is used to capture the dynamics of the air discharge. Figure 3 shows a sequence of ICCD images of the whole area covered by 6×6 units over one complete cycle. The measurements are performed at an air flow rate of 4.0 SLM and $f = 5$ kHz. The ICCD images are obtained with a gate width of 20 ns in steps of 200 ns at the applied voltages of 10 kV (Fig. 3(a)), 12 kV (Fig. 3(b)), 14 kV (Fig. 3(c)), and 15 kV (Fig. 3(d)). The time labeled on each photograph corresponds to the time shown in Fig. 2. In Fig. 3(a), the discharge is triggered at 55.0 μs and ended at 95.0 μs in the NHV cycle while one in the PHV cycle happens at 152.5 μs and ends at 197.5 μs . With the discharge going on, the propagation process images in the NHV and PHV cycle are almost symmetrical, but this is another story at $V_P = 10$ kV. With the applied voltage increasing up to 12 kV, the amplitude of the discharge current reaches 45 mA in the NHV cycle and 60 mA in the PHV cycle. The corresponding ICCD images of propagation process at the delay of 50.0 μs–100.0 μs are obtained during the NHV cycle while those at the delay time of 150.0 μs–200.0 μs during the PHV cycle as shown in Fig. 3(b). In the NHV cycle, appreciable charges accumulate on the surface of the 1.0-mm-thick fibers to form the inverse electric field, lowering the net voltage across the high-voltage and grounded electrode. The original symmetrical propagation in the NHV cycle and PHV cycle is disrupted. A higher voltage increases the expansion of the filament discharge region and shortenes the time required for the occurrence of complete uniformity. Thus, a large-area and homogeneous discharge in PHV cycle is fully covered on the dielectric surface due to the diffusion effect of the discharge filaments.

Figure 3(c) shows the discharge propagation process with an applied voltage of 14 kV. With the increase of applied voltage, a growing number of filament channels are generated. In the propagation process of the discharge, the adjacent filament current channels are merged into one channel with a larger width on the order of μs, forming a type of visually uniform

discharge due to the plasma diffusion effect, which is consistent with the ICCD images. At 65.0 μs in the NHV cycle, it is clearly seen that the regional filament discharge convert into a uniform one. This uniform discharge mode lasts from 65.0 μs to 97.5 μs in the NHV cycle and from 162.5 μs to 200.0 μs in the PHV cycle, and the discharge region covers the whole ITO electrode surface. In this mode, a feedback mechanism at the ground electrode surface is formed. Impinging ions and photons produced secondary electrons which are fed back into the discharge channel. Figure 3(d) shows the discharge propagation process with an applied voltage of 15 kV and $f = 5$ kHz. Compared with $V_P = 10$ kV, 12 kV, 14 kV, the discharge propagation process triggered earlier at 45 μs. With applied voltage increasing, a large amount of power is transferred into the discharge region. At high frequency there appears this situation where an electrode exhibits a preferential location for the repetitive initiation of one or more microfilaments, leading to accumulated thermal instability.

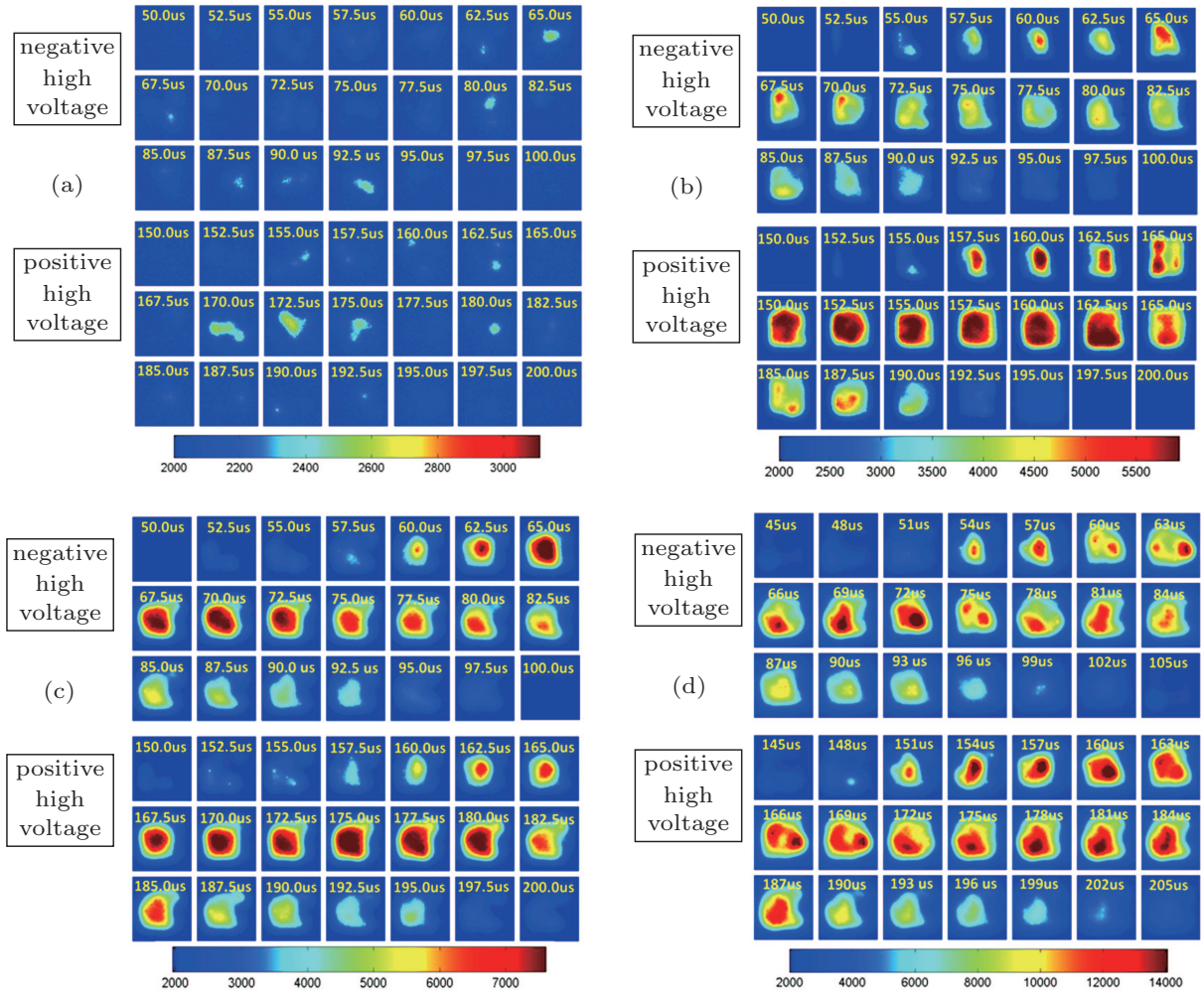


Fig. 3. (color online) High-speed ICCD images of the well-aligned microplasma propagation process over one complete cycle at an air rate of 4 SLM and $f = 5$ kHz. The ICCD images are obtained with a gate width of 20 ns at $V_P =$ (a) 10 kV, (b) 12 kV, (c) 14 kV, and (d) 15 kV.

Figure 4 shows the discharge power as a function of applied voltage and the Lissajous figure obtained at an applied voltage of 12 kV with a repetition frequency of 5 kHz. As stated before, the Lissajous figure can be used to calculate the discharge power, and the area of the closed curve is proportional to the discharge power. With the fixed frequency of 5 kHz, the discharge power slowly increases with the applied voltage varying from 8.0 kV to 15 kV and sharply increases over the applied voltage of 15 kV. The increase in the discharge power indicates an improvement in well-aligned microplasma density, which is well consistent with the propagation process. The well-aligned air plasma generated at $V_P = 14$ kV is utilized for plasma modification of PET and inactivation of *E. coli* cells, and its discharge power is 16 W. indicating a low gas temperature of the well-aligned plasma.

The ICCD images display that a stable and large area diffusion discharge could be achieved in a wide range of discharge voltage. As the discharge voltage increases, the plasma area is significantly enlarged both horizontally and vertically (see Fig. 3). When the discharge voltage increase up to 12 kV, the discharge plasma spreads over the whole dielectric layer surface under the square array electrode, and a large area (about 35 mm×35 mm) of discharge plasma is formed. This behavior can be understood by using a simple model for

the breakdown of the discharge as shown in Fig. 1(d). With the well-aligned array microelectrodes, the localized filament channels are generated with the localized high electron density and energy. Figure 2(e) shows an optical intensity monitored by a PMT at the side of the well-aligned microplasma arrays, with the voltage and current waveforms recorded simultaneously. Apparently, optical intensity signals are consistent with filaments of discharge current on the whole. Furthermore, the filament from a single jet (individual unit) is also investigated. With a high-speed ICCD camera, a diffusing and bright circle ring outside the individual plasma jet unit is continuously seen in the discharge time, in accordance with the above discussion. As already discussed above, the arrays are not triggered simultaneously but show repetitive spatial variations, acting as a mode of filamentary barrier discharge. Usually at a high jet density, jet–jet interactions will be so strong that they can cause repelled or converged jet channels, thus defeating the purpose of forming an array.[29] Difference in plasma ignition can be attributed to jet–jet interactions in general, since the transport of neutral species and UV photons caused by one plasma jet should affect the dynamics of its sounding jets. Less straightforward is, however, the difference in the voltage of plasma ignition, when the plasmas are just triggered and their interactions must be very weak.

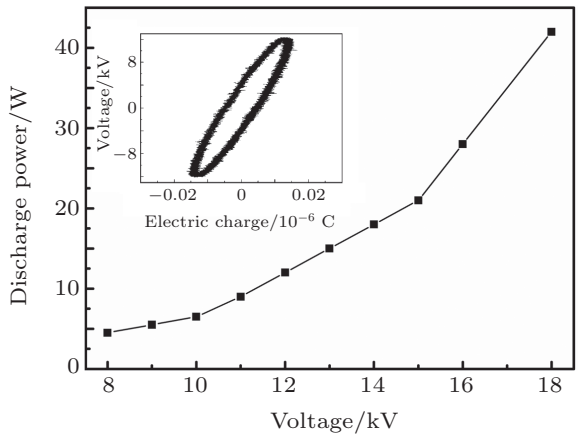


Fig. 4. Discharge power of the well-aligned plasma device as a function of applied voltage and voltage-versus-charge (Lissajous figure in the inset) obtained at an applied voltage of 12 kV with a repetition frequency of 5 kHz.

To overcome the discharge excitation threshold requires the applied voltage U_a to be increased to reach the breakdown voltage U_b over the discharge gap d. U_b is only related to the kind of gas used and the discharge gap d, and can be considered as a constant in this aligned air plasma discharge. Then U_a is given by

$$U_a = U_b + U_d, \tag{1}$$

where

$$U_d = \frac{Q}{c_d} = \frac{\int I\,dt}{C_d}. \tag{2}$$

Here, U_d is the voltage difference between the upper and lower surfaces of the dielectric layer; C_d is the electric capacity of dielectric; $\int I\,dt$ is the integral of breakdown current, and represents the electrical charges accumulated on the dielectric layer surface. With the increase of the applied voltage, Q value can be improved, also indicating the increase of the density of electrical charges. Figure 1(d) shows the discharge and diffusion models of the microplasma arrays. In the negative half period, electrons are accelerated out of the microplasma units towards the grounded electrode. They reach the excitation threshold at the top of the single jet unit, leading to a spacious emission feature (expanding). In the positive half period, electrons are accelerated from the ground electrode into the microplasma units. In addition, increasing the discharge voltage can contribute to the increase of reduced electric field E/N, which leads to an increase in the density of the high-energy electrons. Accordingly, more electron avalanches can be obtained in the discharge gap. Additionally, a greater number of excited molecules and ions can be generated in a larger region. Therefore, the discharge becomes more intense and the plasma area expands. For more details of streamer propagation mechanism, the literature[30] is strongly recommended.

3.2. Large-area surface modification of materials

Such a diffusing and large-area microplasma with low temperature is highly suitable for large-area surface modification of materials or biological sterilization. The plasma has no detrimental effect on the heat-sensitive material due to its low gas temperature, which is indicated by the discharge power from Lissajous figures; the discharge power is calculated to be about 16 W. The sessile water-drop contact angles of PET samples are plotted as a function of the plasma treatment time as shown in Fig. 5.

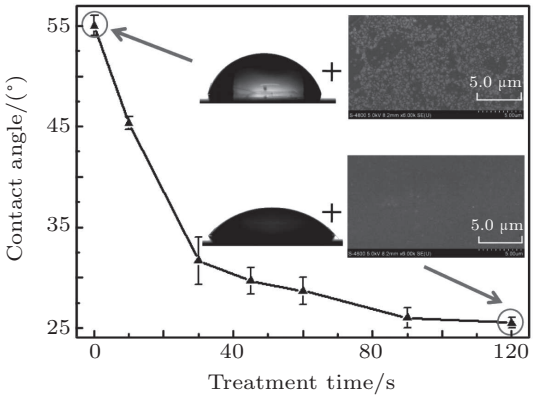


Fig. 5. Sessile water-drop contact angles as a function of the plasma treatment time of PET samples and the typical SEM images for platelets adhering to the untreated and plasma-activated PET samples.

Plasma treatment may result in a hydrophobic surface of PET sample and have a great effect on the contact angle of PET sample. The contact angle of PET sample decreases markedly from (55.0±1.0)° to (25.5±0.5)° with the plasma treatment time being 2 mins. Figure 5 also shows the typical

SEM images for platelet adhering to the untreated and plasma-treated PET sample respectively. Clearly, there is a high density of platelets adhering to the untreated PET sample, whereas no adhesion of platelets was observed on the plasma-treated PET sample, possibly as a result of the hydrophilic property of PET surface. A hydrophobic recovery of plasma-activated PET sample is observed under ambient conditions, where after 3-days aging the water contact angle for the sample treated in air is raised to 39° and the adhesion of platelets on PET sample is also significantly affected.

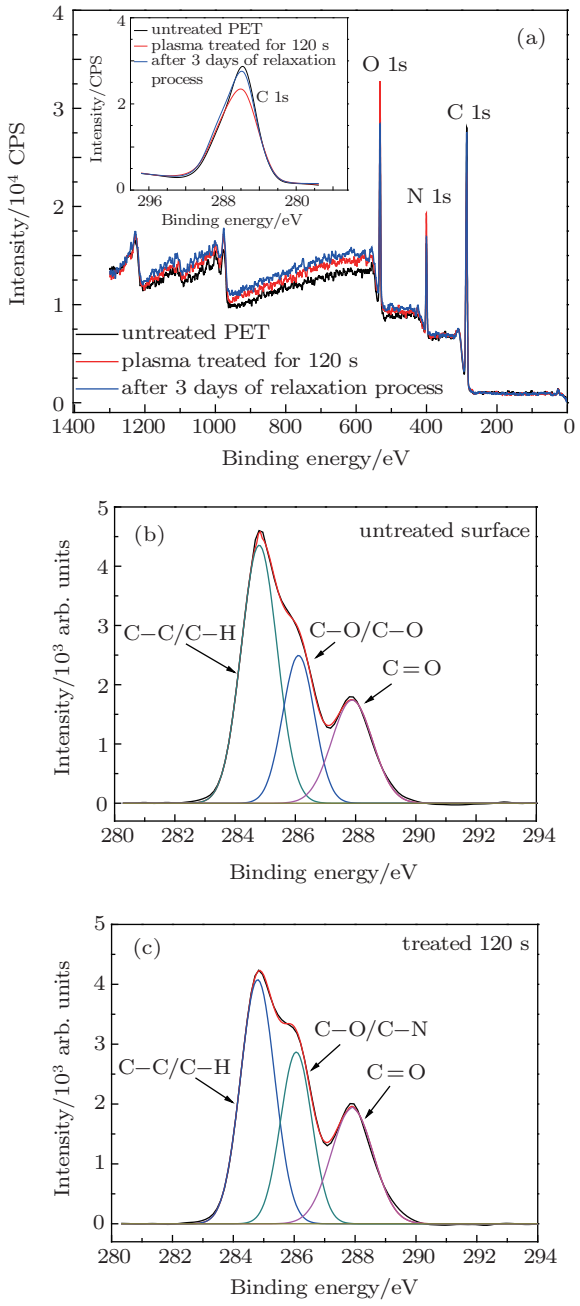


Fig. 6. (color online) (a) Survey XPS spectra of untreated (virgin), air plasma treated PET surfaces and after 3-days relaxation process. High-resolution C 1s spectra for (b) untreated and (c) plasma-treated PET polymers.

The obvious differences in contact angle and platelet adhesion between untreated and plasma-activated PET samples are attributed to their surface change in chemical composition and bonding environment. Survey-scan XPS spectra show that carbon, nitrogen and oxygen are existent, and they are the built blocks of the film. Figure 6(a) shows that the surface concentrations of oxygen and nitrogen in the treated PET sample increase from the initial 18.6% and 13.3% to 22% and 15.2%, respectively, while the carbon concentration decreases from 67.8% to 62.8%. A decrease in the C content indicates that H atoms at PET surface can be replaced by N- or O-containing reactive species generated in the air plasma jet. Interestingly, after 3-days aging of relaxation process, the concentrations of these elements on plasma treated samples essentially return to their original levels: for each of the samples, its carbon concentration rises to 67.1% and oxygen and nitrogen concentration decrease to 19.2% and 13.7% respectively. The XPS C1s spectrum for the untreated PET sample is shown in Fig. 6(b). The carbon spectrum may be decomposed into three features.[31] The peaks at 286.4 eV and 288.8 eV arise from –C–O/–C–N and –C=O groups respectively, while the peak at 284.8 eV is assigned to the –C=C– in the aromatic ring. The XPS C1s for the PET sample treated with the air plasma jets is shown in Fig. 6(c). Plasma treatment results in the changes in intensity and width of these three peaks. The increases in intensity of these peaks at 286.4 eV and 288.8 eV, suggest that –C–O/–C–N and –C=O groups can be formed due to the plasma treatment. When the platelet-rich blood plasma is applied onto the well-activated surface of PET, the molecular adsorption mechanism of plasma protein becomes different from that on the untreated sample. With the principle of "like dissolves like", H_2O molecules can easily be adsorbed onto the surface of the plasma-activated PET sample while plasma proteins tend to be adsorbed onto the untreated PET surface.

3.3. Large-area bacterial inactivation

Figure 7 shows the images of (a) plasma-untreated (control) *E. coli* sample, and the *E. coli* samples treated by well-aligned air plasma for (b) 10 s, (c) 30 s, (d) 1 min, and (e) 2 min. The marked square areas indicate the well-aligned microplasma regions above the *E. coli* samples. All plasma-treated samples are cultivated for 24 h in a 37-°C thermostat after plasma treatment. The blank area in the petri dish rapidly increases when the plasma treatment time increases from 10 s to 2.0 min, which confirms that the atmospheric-pressure air microplasma results in the rupturing of *E. coli* cells. It can be seen that most of the *E. coli* cells in the Petri dish in the marked area are killed after the 2-min plasma treatment. Moreover, a large-area and homogeneous inactivation of *E. coli* cells in the marked area can be formed, which is attributed to the plasma uniformity on the dielectric surface. The plasma-activated species can come into direct contact with the *E. coli* samples and efficiently kill *E. coli* cells in the Petri dish. The survival

rate of the *E. coli* cells is plotted as a function of the plasma treatment time as shown in Fig. 8. Increasing V_P from 10 kV to 14 kV leads to a noticeable improvement in the efficiency of bacterial inactivation for a given treatment time. The improved inactivation efficiency is likely due to an increase in the discharge power. When the plasma treatment time increases from 10 s to 60 s, the inactivation efficiency is also greatly improved. This improvement gradually slows down with the further increase of treatment time. The inactivation efficiency can reach up to almost 100% within 2-min treatment.

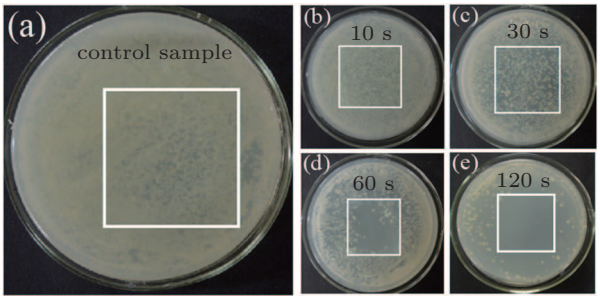


Fig. 7. (color online) Images of (a) plasma-untreated (control) *E. coli* sample, the samples treated by the well-aligned plasma for (b) 10 s, (c) 30 s, (d) 60 s, and (e) 120 s. The marked area indicates the air microplasma area above the *E. coli* sample.

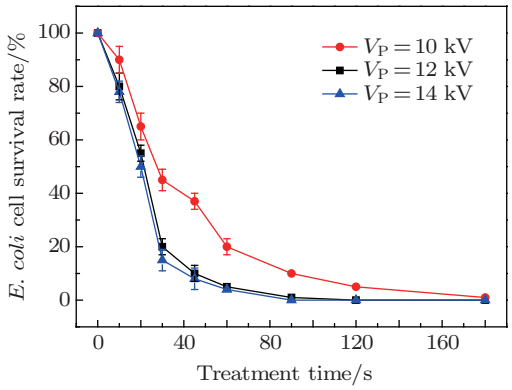


Fig. 8. (color online) Plots of survival rate of *E. coli* versus processing time, obtained at various applied voltages.

The optical emission spectra (OES) with a wavelength range from 200 nm to 500 nm at various discharge voltages are collected as shown in Fig. 9. The optical fiber is fixed to be 3 cm away from the broadside of the discharge region. These OES spectra are dominated by N_2 (C–B) and OH. The excited N_2 (C–B) and reactive OH species are mainly produced via the energetic collisions of electrons with N_2, O_2, and H_2O molecules.[21] An increase of discharge voltage applied to the well-aligned plasma device contributes to high density of OH or excited N_2 (C–B) radicals. Our OES measurements are well consistent with the observations from bacterial experiments for the reason that these plasma-generated species are very reactive and could be important contributors in the sterilization processing.

In this paper, the well-aligned microplasma operating at room temperature is designed for the large-area surface modification of heat-sensitive PET polymers and inactivation of resistant *E. coli* cells. This design can generate a kind of visible large-area and homogeneous discharge, resulting in a uniform surface interaction of plasma species with PET polymers and *E. coli* cells. It is suggested that various plasma-activated particles including charged species, UV photons and radicals, which are natural carriers of energy, play the leading role in the plasma modification and inactivation process, provided they excite a polymer, or break the chemical bonds at the polymer surface or directly reach *E. coli* cells.

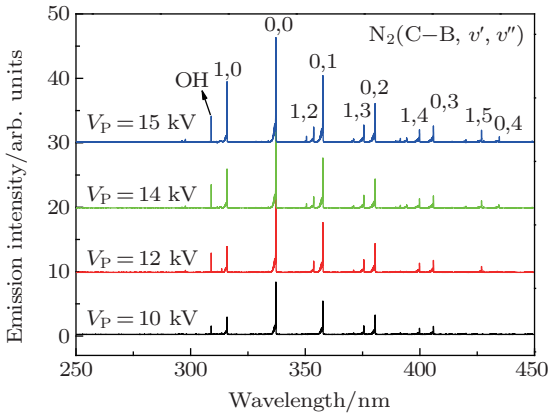


Fig. 9. (color online) Typical emission spectra of air surface diffusion discharge at various discharge voltages.

The surface interactions of both radicals and energetic ions with the PET surface can create the dangling bonds and contribute to the incorporation of oxygen and nitrogen.[32] Our SEM measurements also show that the surface topography of the PET sample is not influenced by the plasma treatment. The temperature of the plasma-treated PET sample is measured with an infrared radiation thermometer, and it is usually lower than 40 °C. Therefore, the stable and homogeneous air plasma operating at room temperature does not cause damage to the heat-sensitive polymers and is suitable for the large-area surface modification of polymers in biomedical application.

Charged species are also supposed to induce the rupture of the outer membrane of bacteria cells.[33,34] The electrostatic force caused by charge accumulation on the outer surface of the cell membrane can overcome the tensile of the membrane and cause its rupture. Metastable or excited species can emit UV photons for plasma inactivation. The UV radiation with doses of several milliwatts per cm^2 may cause lethal damage to cells.[35] However, no UV radiation in the 200 nm–300 nm wavelength range is observed by our OES measurement. It is generally believed that UV photons do not play a major role in the inactivation process by atmospheric-pressure cold plasma.[22,33,34] The O radicals are believed to play a crucial role in the plasma inactivation of microorganism.[35,36] Moreover, the frequent collisions between O radicals and O_2 molecules can result in the production of ozone ($O + O_2 + M \rightarrow O_3$).[4] Unsaturated fatty acids and sulfhydryl groups are readily oxidized with ozone. These

oxidization process may lead to the inactivation of microorganisms and bacterial spores. The presence of these plasma-activated species can therefore compromise the function of the cell membrane which serves as a barrier against the transports of ions and polar compounds into and out of the cells.

4. Summary

The well-aligned microplasma device designed in this study is successfully utilized to generate a large-area and homogeneous plasma at atmospheric pressure in air. The surface charges from microplasma jet units may form the electric field along the quartz surface, and tend to be distributed and diffuse uniformly at an applied voltage in the range of 12 kV–14 kV, which leads to the uniform and large-area surface discharge for modifying the heat-sensitive PET polymers and inactivation of *E. coli cells*. This technique demonstrates its potential for surface inactivation in biomedical application, as well as large-area surface modification in industrial application.

References

[1] Morfill G E, Kong M G and Zimmermann J L 2009 *New J. Phys.* **11** 115011

[2] Zhang X H, Liu D P, Zhou R W, Song Y, Zhang Q, Niu J H, Fan H Y and Yang S Z 2014 *Appl. Phys. Lett.* **104** 043702

[3] Laroussi M, Mendis D A and Rosenberg M 2003 *New J. Phys.* **5** 41

[4] Ehlbeck J, Schnabel U, Polak M, Winter J, von Woedtke Th, Brandenburg R, von dem Hagen T and Weltmann K D 2011 *J. Phys. D: Appl. Phys.* **44** 013002

[5] Aita T, Ogawa K, Saito Y, Sumiyoshi Y, Higuchi T and Sato S 2010 *Surf. & Coat. Technol.* **205** 861

[6] Huang C, Hsu W T, Liu C H, Wu S Y, Yang S H, Chen T H and Wei T C 2009 *IEEE Trans. Plasma Sci.* **37** 1127

[7] Pothiraja R, Bibinov N and Awakowicz P 2010 *J. Phys. D: Appl. Phys.* **43** 495201

[8] Ostrikov K, Neyts E C and Meyyappan M 2013 *Adv. Phys.* **62** 113

[9] Bussiahn R, Brandenburg R, Gerling T, Kindel E, Lange H, Lembke N, Weltmann K D, von Woedtke Th and Kocher T 2010 *Appl. Phys. Lett.* **96** 143701

[10] Zhang X H, Liu D P, Song Y, Sun Y and Yang S Z 2013 *Phys. Plasmas* **20** 053501

[11] Hsu C C and Yang Y J 2010 *IEEE Trans. Plasma Sci.* **38** 496

[12] Wu S, Lu X, Xiong Z and Pan Y 2010 *IEEE Trans. Plasma Sci.* **38** 3404

[13] Lu X, Xiong Z, Zhao F, Xian Y, Xiong Q, Gong W, Zou C, Jiang Z and Pan Y 2009 *Appl. Phys. Lett.* **95** 181501

[14] Moisan M, Barbeau J, Moreau S, Pelletier J and Tabrizian M 2001 *International J. Pharmaceutics* **226** 1

[15] Kong M G, Kroesen G, Morfill G, Nosenko T, Shimizu T, van Dijk J and Zimmermann J L 2009 *New J. Phys.* **11** 115012

[16] Laroussi M, Leipold F 2004 *Int. J. Mass Spectrometry* **233** 81

[17] Eto H, Ono Y, Ogino A and Nagatsu M 2008 *Appl. Phys. Lett.* **93** 221502

[18] Eden J G, Park S J, Cho J H, Kim M H, Houlahan T J and Li B 2013 *IEEE Trans. Plasma Sci.* **41** 661

[19] De Geyter N, Morent R, Gengembre L, Leys C, Payen E, Vlierberghe S V and Schacht E 2008 *Plasma Chem. Plasma Process.* **28** 289

[20] Song Y, Liu D P, Ji L F, Wang W C, Zhao P C, Quan C S, Niu J H and Zhang X H 2012 *Plasma Process. Polym.* **9** 17

[21] Zhou R, Zhang X, Bi Z and Zong Z 2015 *Appl. Environ. Microbio.* **81** 01287

[22] Choi J H, Lee T I, Han I, Baik H K, Song K M, Lim Y S and Lee E S 2006 *Plasma Sources Sci. Technol.* **15** 416

[23] Bibinov N K, Fateev A A and Wiesemann K 2001 *J. Phys. D: Appl. Phys.* **34** 1819

[24] Linss V, Kupfer H, Peter S and Richter F 2004 *J. Phys. D: Appl. Phys.* **37** 1935

[25] Lu X, Jiang Z, Xiong Q, Tang Z, Hu X and Pan Y 2008 *Appl. Phys. Lett.* **92** 81502

[26] Sands B L, Ganguly B N and Tachibana K 2008 *Appl. Phys. Lett.* **92** 151503

[27] Zhu Y, Takada T, Inoue Y and Tu D 1996 *IEEE Trans. Dielectr. Electr. Insul.* **3** 460

[28] Li X, Yuan N, Jia P and Chen J 2010 *Phys. Plasma* **17** 093504

[29] Cao Z, Nie Q, Bayliss D and Kong M 2010 *Plasma Sources Sci. Technol.* **19** 25003

[30] Lu X, Naidis G V, Laroussi M and Ostrikov K 2014 *Phys. Rep.* **540** 123

[31] Zhou R, Zhang X, Zong Z, Yang Z, Li J, Liu D and Yang S 2015 *Chin. Phys. B* **24** 085201

[32] Sakamoto C, Ayotte G, Turgeon S, Massines F and Laroche G 2009 *Langmuir* **25** 9432

[33] Laroussi M 2009 *IEEE Trans. Plasma Sci.* **37** 714

[34] Walsh J L and Kong M G 2008 *Appl. Phys. Lett.* **93** 111501

[35] Norman A 1954 *J. Cell Comp. Phys.* **44** 1

[36] Sun P, Sun Y, Wu H, Zhu W, Lopez J L, Liu W, Zhang J, Li R and Fang J 2011 *Appl. Phys. Lett.* **98** 021501